OPEN

Growing perovskite into polymers for easy-processable optoelectronic devices

Sofia Masi[1,2]*, Silvia Colella[3]*, Andrea Listorti[2,3], Vittoria Roiati[2,4], Andrea Liscio[5], Vincenzo Palermo[5], Aurora Rizzo[3] & Giuseppe Gigli[1,2,3]

[1]Dipartimento di Matematica e Fisica ''E. De Giorgi'', Universita' del Salento, Via per Arnesano, 73100 Lecce, Italy, [2]Center for Bio-Molecular Nanotechnology - Fondazione Istituto Italiano di Tecnologia, Via Barsanti, 73010 Arnesano (Lecce), Italy, [3]NNL – National Nanotechnology Laboratory, CNR Istituto Nanoscienze, Distretto Tecnologico, Via Arnesano 16, 73100 Lecce, Italy, [4]Dept. of Physics, Politecnico di Milano, p.zza Leonardo da Vinci 32, Milano, Italy, [5]Istituto per la Sintesi e la Fotoreattività CNR, via Gobetti 101, Bologna, 40120, Italy.

Here we conceive an innovative nanocomposite to endow hybrid perovskites with the easy processability of polymers, providing a tool to control film quality and material crystallinity. We verify that the employed semiconducting polymer, poly[2-methoxy-5-(2-ethylhexyloxy)-1,4-phenylenevinylene] (MEH-PPV), controls the self-assembly of $CH_3NH_3PbI_3$ (MAPbI$_3$) crystalline domains and favors the deposition of a very smooth and homogenous layer in one straightforward step. This idea offers a new paradigm for the implementation of polymer/perovskite nanocomposites towards versatile optoelectronic devices combined with the feasibility of mass production. As a proof-of-concept we propose the application of such nanocomposite in polymer solar cell architecture, demonstrating a power conversion efficiency up to 3%, to date the highest reported for MEH-PPV. On-purpose designed polymers are expected to suit the nanocomposite properties for the integration in diverse optoelectronic devices via facile processing condition.

N owadays hybrid halide perovskites allow outstanding photovoltaic performance[1] and represent one of the most appealing materials for various optoelectronic applications, such as light emitting diodes[2] and lasers[3–5]. Hybrid perovskites are solids formed by an inorganic framework, usually a metal halide, intercalated by organic cations filling its voids, resulting in a polycrystalline material with octahedral arrangement[6]. The formation of the crystals occurs spontaneously, driven by the self-assembly of the two precursors upon deposition[7,8]. Despite this great potential, the deposition of hybrid perovskites remains an important challenge with several and major limitations in terms of film growth and morphology control[9]. Although inject printing and spray coating has been recently demonstrated on small area devices[10,11], these issues could interfere with the scale-up of perovskite-based devices towards low-cost technologies such as roll-to-roll, and may impede their rapid implementation for entering the market. Polymer-based technologies, on the other hand, possess all the processing requirements foreseeing feasible mass scale production, yet still limited by the lack of high-performing materials. In polymer photovoltaic (PV), in fact, despite the huge efforts devoted to the improvement of materials and device structure[12], the achieved performances and the available synthetic protocols do not fulfill the market requirements. In particular, bulk hetero-junction (BHJ) solar cells improvements are limited by the mostly employed electron acceptor fullerene derivative, phenyl-C61-butyric acid methyl ester (PCBM), penalized by the onerous production cost[13], difficulty of forming continuous and controllable domains in the polymer film and almost complete transparency to sunlight[14].

In this scenario we propose a novel strategy to control the perovskite growth and film- forming properties by exploiting polymers as templating agent. We have successfully verified the self-assembly of MAPbI$_3$ crystals in the MEH-PPV matrix, realizing a new class of nanocomposite for whom we achieve high quality and smooth thin film, deposited in one straightforward step.

As a demonstration that our nanocomposite can act as active layer in optoelectronic devices, we fabricated a BHJ-like solar cell. Remarkably, the MEH-PPV:MAPbI$_3$ based device shows a PCE of 3%, representing the highest efficiency ever reported for MEH-PPV polymer, reaching, for the first time, the successful replacement of fullerene species with MAPbI$_3$ perovskite in a polymeric solar cell. Photo-induced absorption[15] and scanning Kelvin Probe Force Microscopy (KPFM)[16], further reveal the photoconversion mechanism occurring in the nanocomposite with MAPbI$_3$ acting as electron-acceptor species.
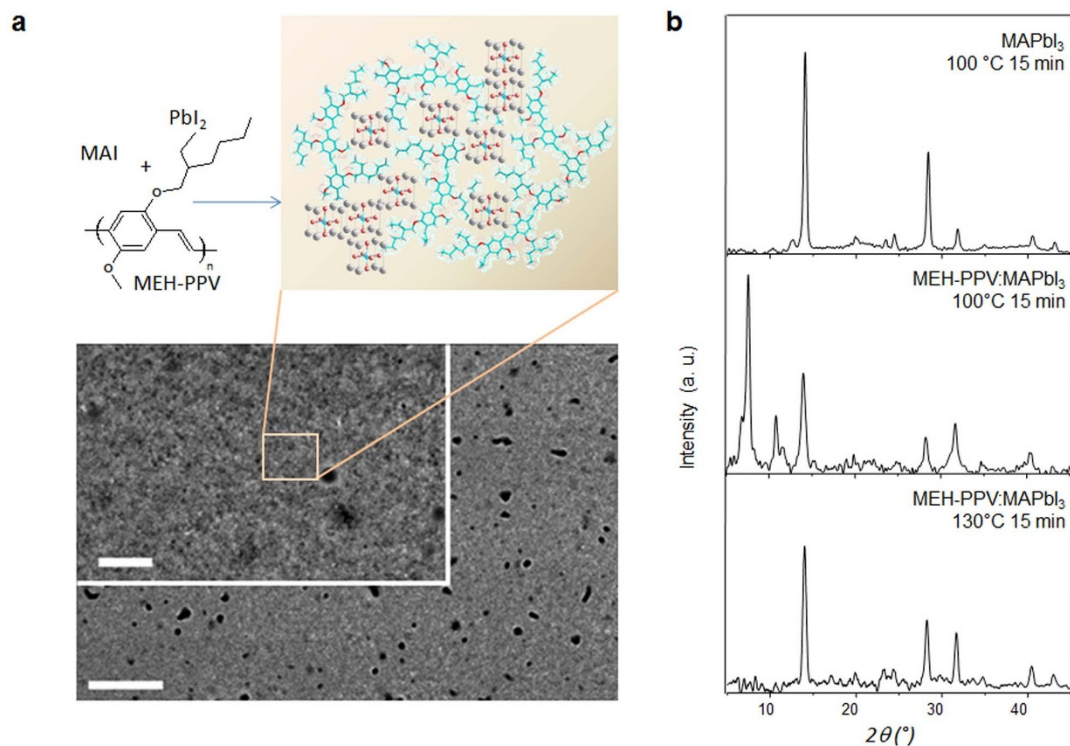
Figure 1 | SEM images of nanocomposite and XRD diffraction patterns of the active layer. (a), Nanocomposite precursors and SEM top view of MEH-PPV : MAPbI$_3$ 1 : 36 (by weight) blended film spin-cast from THF/DMF/tBuPy (2,5 : 1 : 1) solution at low and high magnification (Inset); scale bars correspond to 2 μm and 500 nm respectively. (b), XRD patterns of MAPbI$_3$ film and MEH-PPV:MAPbI$_3$ film as a function of annealing conditions. The amorphous contributions from polymer and substrate are subtracted to the diffractograms.

Among the extensive library of commercially available semiconductor polymers, the choice of the p-type donor MEH-PPV (Fig. 1a), widely employed as active material in optoelectronic devices[17–19], over more performing classes of polymers such as polythiophenes, is driven by the suitability of some of its properties to be compatible with perovskite material. In particular, besides the one-dimensional electronic structure, mechanical plasticity and film-forming capability, its convenient solubility in polar non-aromatic organic solvent, such as tetrahydrofurane (THF) and the stable coexistence with the perovskite precursors in solution, is an essential requirement to allow the growth of 3D perovskites into a semiconductor polymer.

Results

Formation of nanocomposite and structural analysis. Aiming to demonstrate the spontaneous formation of perovskite in the polymer matrix and to control the structure of the resulting nanocomposite, we preliminarily explored different processing conditions, additives and solvents for the deposition of the active layer. The nanocomposite film is obtained from a MEH-PPV, methylammonium iodide (MAI) and lead iodide (PbI$_2$) blend solution (see sketch in Fig. 1a) in a binary mixture of solvents THF:DMF (tetrahydrofurane: dimethylformamide). Furthermore, 4-$tert$-Butylpyridine (tBuPy) (see methods for details) is added as additive to the mixture to stabilize the components in solution and lead to an optimized morphology[20]. Scanning Electron Microscopy (SEM) investigations of the nanocomposite show a rather smooth film (Fig. 1a) compared to a typical pristine perovskite. In particular, SEM analysis highlights the presence of few large structures on the sample surface, and a rather uniform active layer underneath, likely given by a fine mixture of MEH-PPV and perovskite domains (Inset of Fig. 1a). In Fig. 1b we show the X-ray diffraction (XRD) pattern of pristine MAPbI$_3$ and MEH-PPV: MAPbI$_3$ nanocomposite films on glass substrates. The main diffraction peaks, assigned to the (110), (220), (312) and (224)

faces, are common and found at identical angles, namely 14.05°, 28.38°, 31.74° and 40.63°, for both the pristine perovskite and the nanocomposite, confirming the formation of perovskite crystals in the polymer matrix with the same tetragonal structure[21,22]. The inclusion of a layered perovskite in a polymer has been previously achieved, for a very different purpose, in a study on the dewetting behaviour of insulating polystyrene film filled with the layered (C$_6$H$_5$C$_2$H$_4$NH$_3$)$_2$PbI$_4$[23], but the growth of 3D perovskites into a semiconductor polymer has never been verified before. Interestingly, the diffraction pattern corresponding to the MEH-PPV:MAPbI$_3$ active layer, annealed at 100°C, shows the presence of two additional XRD peaks at low angles (7.64° and 10.94°), which has been attributed to the formation of a tBuPy-PbI$_2$-MAI intermediate phase[22,24], in the recent findings envisaged by Seok et al.[21] for a perovskite-dimethylsulfoxide (DMSO) system, where DMSO is likewise used as solvent additive. Such peaks decrease in intensity by increasing the post-deposition annealing temperature from 100°C to 130°C, as shown in Fig. 1b, revealing the transition nature of this state.

To further address the role of tBuPy, the FT-IR spectra of MEH-PPV and MEH-PPV:MAPbI$_3$ blend, are measured to determine the characteristic vibrational modes of perovskite and tBuPy and to identify their presence in the polymer matrix. Samples are prepared both with tBuPy additive and annealed at 100°C (Supplementary Fig. S1) to avoid thermal stress of MEH-PPV[25,26] and according to the optimal annealing temperature for perovskite. The comparative analysis of the FT-IR spectra only shows the tBuPy stretching and bending modes (indicated with ashes Supplementary Fig. S1) in the MEH-PPV:MAPbI$_3$ sample, suggesting that in presence of the pure polymer the annealing treatment induces the tBuPy evaporation. Nevertheless it is not enough to break the non-covalent interactions between tBuPy and the perovskite precursors in the hybrid nanocomposite. Atomic Force Microscopy (AFM) on MEH-PPV:MAPbI$_3$ blend either with or without tBuPy additive

(Supplementary Fig. S2) is performed to verify the beneficial role of the intermediate *t*BuPy-PbI$_2$-MAI complex in obtaining a smooth active layer. AFM characterization confirms that the film with *t*BuPy has a fairly flat morphology with few bigger aggregates resulting in an overall root mean square roughness R$_{rms}$ of 28 ± 3 nm, whereas the blend without additive shows a higher R$_{rms}$ of 35 ± 5 nm.

Photovoltaic application. The MAPbI$_3$: MEH-PPV nanocomposite, given the smooth morphology and the fine dispersion of the perovskite in the polymer matrix, was tested in an inverted photovoltaic device to explore its capability of photogenerate and extract charges. The employed solar cell geometry and the energy alignment of the two materials, namely a donor/acceptor couple, is shown in Fig. 2a,b. The MEH-PPV, MAI and PbI$_2$ blend in THF:DMF and *t*BuPy additive is deposited in one step *via* spin-coating onto a fluorine-doped tin oxide, previously coated with a compact layer of TiO$_2$ that acts as electron-selective contact. The evaporation of *N,N,N′,N′*-Tetrakis(4-methoxyphenyl)benzidine (MeO-TPD) on the blend ensures the selective funnel of the holes towards Au anode[27,28], as evidenced by the PV performance at different MeO-TPD thicknesses reported in Table S1.

The J-V curves for the best-performing device in dark and under standard AM1.5G solar spectrum illumination conditions are shown in Fig. 2c. Furthermore, in the Supplementary Information (Table S1) we report a summary of device performances in phase of optimization, at different annealing temperature and for different weight ratio of MEH-PPV : MAPbI$_3$. We observe that exceeding 1 : 36 polymer : perovskite (until 1 : 70) results in a very inhomogeneous film

and, consequently, paths for charge recombination are increased. If the film is too poor in perovskite (MEH-PPV : MAPbI$_3$ = 1 : 18) the efficiency of solar cell drops as well, due the limited light harvesting capability (Table S1).

Most notably, the best performing MEH-PPV:MAPbI$_3$ based solar cells shows V$_{oc}$ = 0.81 V, J$_{sc}$ = 9.11 mA/cm^2, FF = 0.36 yielding to a PCE of 3.0%, which is the highest among the previously reported MEH-PPV based BHJ devices[29,30]. This result prefigures a promising perspective for the employment of customized photoactive polymers soluble in polar and green solvents, such as water, to be integrated in nanocomposite based solar cells. The use of more suitable polymers with optimized properties and carrier mobility can indeed outperform our concept device, being the fill factor most probably limited by the unbalanced mobility of perovskite and MEH-PPV polymer. Moreover, it could be beneficial to protect perovskite against moisture[31], which is fundamental to improve the stability of perovskite based devices.

Interestingly, a negligible difference exists between forward and reverse scan in the J-V characteristics (Supplementary Fig. S3), evidencing how the implementation of the perovskite in a poymer matrix can minimizes the problem of hysteresis, which is known to affect most of the perovskite-based devices. This phenomenon is frequently detected in perovskite-based solar cells and has been hypothetical attributed to perovskite giant capacitance[32], defect physics at oxide interface, polarization, or to the presence of free mobile ions[33]. The peculiar formation of the perovskite in the organic polymer template impacts on the physics of the material interface defects, as well as on the domains dimensions, which are found to be considerably small in
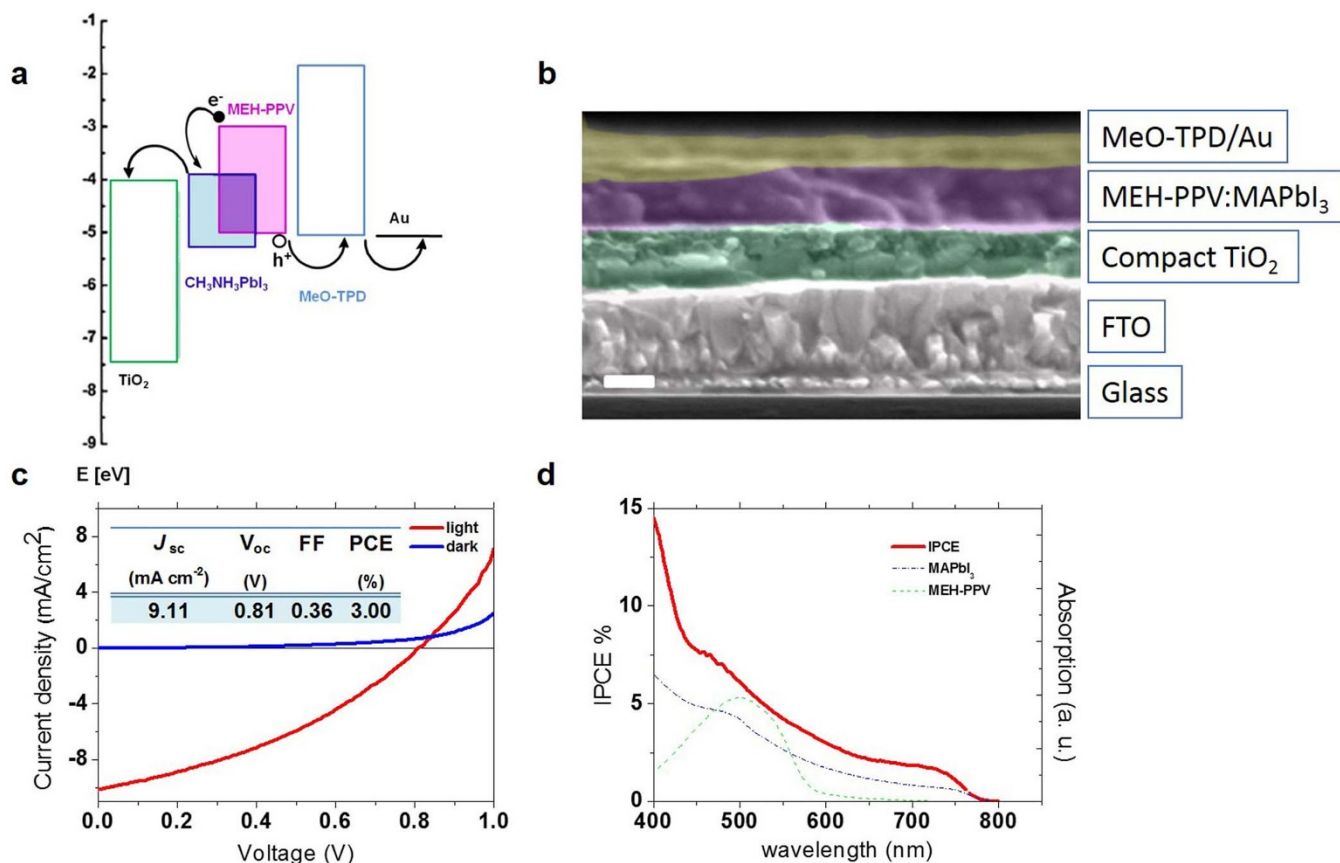

Figure 2 | Structure of polymer, nanocomposite solar cell architecture, and photovoltaic performance. (a), Energy level diagram of the PV components. (b), Cross-sectional SEM view of a completed photovoltaic device with MEH-PPV: MAPbI$_3$ (scale bar 300 nm). Individual layer are indicated on the right. (c), Current density vs. applied bias (J-V) characteristics under AM1.5 G (100 mW·cm^{-2}) simulated solar illumination (red line) and in the dark (blue line) for the MEH-PPV: MAPbI$_3$ based solar cells and (d), IPCE spectrum for the same device and normalized absorption spectra of the MEH-PPV and MAPbI$_3$.

the active layer, as gathered from SEM cross section (Fig. 2b). In the image of the complete device, the polymer and perovskite phases cannot be clearly distinguished over the active layer thickness, therefore resulting in a homogeneous component mixture. We consequently hypothesize that MAPbI$_3$ small domains are included in the polymer matrix leading to homogeneous and nano-textured morphology.

These characteristics could influence the capability of the material to build up a capacitance and in general to accumulate the charge. Accordingly, the absence of hysteresis here could be related to the extended interface between the perovskite and the polymer, which likely favours the efficient charge extraction from the perovskite[21,34].

Comparing the incident photon to current efficiency (IPCE) with the absorption spectra of the MAPbI$_3$ and MEH-PPV (Fig. 2d) and with an analogous device built in the same configuration without MEH-PPV (Fig. S4), we observe the contribution of both materials to the photo-conversion mechanism in the PV device, as demonstrated by photo-induced absorption (see above). Such a hint suggests that the polymer does not simply act as a template matrix for the perovskite growth but also functions as active specie.

Nanocomposite photo-physical characterization. To shine light on the mechanism behind the photo-physical properties, we monitored in-situ the surface potential of the MEH-PPV:MAPbI$_3$ interface by mapping the charge photogeneration[35] with KPFM technique. Despite the quite uniform morphology (Fig. 3a), the KPFM measurement under illumination (Fig. 3c) reveals well defined patches at different surface potential imputable to the presence of interfacial region where photocharges are generated. Both KPFM images are directly correlated with the morphology by superimposing the gradient filter of the corresponding topographic image (white levels in fig. 3b and blue one in fig. 3c). The gradient filter provides to visualise the level curve corresponding to the main clusters.

The scan of the sample performed in dark, instead, does not show appreciable inhomogeneity (Fig. 3b) suggesting a fine intermixing of MEH-PPV and MAPbI$_3$ in the film, with grain sizes smaller than 20–30 nm, corresponding to the lateral resolution of the technique in our experimental conditions, in accordance with SEM characterization. Due to the nanometric size of grain comparable to the photocharges recombination length[36], we can consider the entire grain within the interface region between the two materials. In Fig. 3c, the bright and dark patches at different potential correspond to electron-accepting and electron-donating domains respectively, which we assign to perovskite-rich and polymer-rich micro-phases within the nano-textured morphology.

Being MEH-PPV/MAPbI$_3$ blend a uniform 3D network of small grains (respect to the lateral resolution), we observed a general shift of the measured potential corresponding to the average of the local variation of the charge density. We can further observe the presence of large aggregates distinguished in the AFM topography (Fig. 3a), as well as in the SEM image (Fig. 1a), attributed to polymer aggregation.
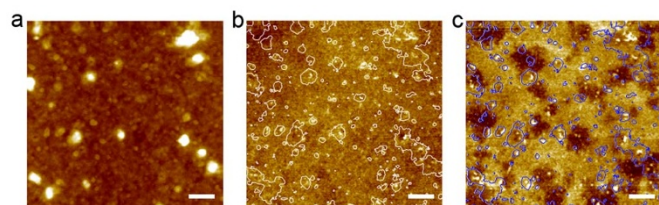

Figure 3 | Kelvin probe force microscopy study on polymer:perovskite active layer. (a), AFM and corresponding KPFM images of polymer:perovskite blend (MEH-PPV : MAPbI$_3$ in weight 1 : 36) acquired in (b), dark and (c) light. Z-range: (a) 200 nm, (b,c) 80 mV. (Scale bar 2 μm) The white and blue closed curve drawing in Fig. b and c are guide to the eyes, mirroring the topography in Fig. 3a.

These large structures do not vary their surface potential, pointing out that only small grains participate to the charge generation process.

Photo-physical analysis is performed to investigate interfacial interaction between the two components of the blend. The absorption spectrum of MEH-PPV:MAPbI$_3$ blend coincides with the sum of its components (Fig. 4a), accounting for the absence of strong interaction in the ground state. Upon excitation of both components in the high-energy region of the spectrum (509 nm), photoluminescence (PL) of MEH-PPV (τ = 330 ps, in line with literature[37]) is largely quenched (above 95%) in blend with MAPbI$_3$ (τ < 40 ps, our instrumental resolution) (Fig. 4b,c). This result clearly indicates the formation of additional deactivation pathways for the localized excited state of the polymer, which can be ascribed to the electron and/or the exciton transfer from MEH-PPV to the MAPbI$_3$. Selectively exciting the perovskite species at 635 nm, we find that its PL is fairly quenched (65%) in the nanocomposite system compared to the pristine perovskite film covered by inert poly(methylmethacrylate) (PMMA) polymer (Fig. 4d). Interestingly, performing PL measurement on a nanocomposite blend of MAPbI$_3$ and the PMMA we notice a radiative deactivation which differs from the bilayer MAPbI$_3$/PMMA (30% reduction), Fig. 4d. This observation agrees with other reports, which have already shown that perovskite PL quenching cannot be straightforwardly associated to charge extraction, but can also be related to crystal growth and neighbouring materials. It has been demonstrated, in fact, that photoluminescence varies in flat or mesoporous architectures and depending on the substrate where the perovskite is deposited[38–40].

We employ quasi steady-state photo-induced absorption (cw-PIA) spectroscopy to clarify this last observation and determine the presence of long-living photo excited species in model samples. Fig. 5 shows the spectra of the perovskite-polymer mixture and of the pristine materials, deposited in the same conditions and from the same solvents onto glass substrates and encapsulated.

Cw-PIA spectra of isolated MAPbI$_3$ and MEH-PPV are reported in Fig. 5a and b respectively. Perovskite spectrum shows the well-known positive peak at 760 nm attributed to the bleaching of the absorption on-set[4,41]. MEH-PPV film on glass shows a very small negative feature which can be assigned to a PL bleaching induced by the probe light, being the triplet state of MEH-PPV located around 900 nm and not detectable at room-temperature[42].

The nano-composite is excited at two different wavelengths, 488 nm and 700 nm, with the same incident power, to isolate the contribution of the perovskite component to the PIA spectra; in fact in the high-energy region of the spectra (488 nm excitation) both the MAPbI$_3$ and the MEH-PPV contribute to the light harvesting, whereas in the low-energy region (700 nm) only the perovskite is absorbing. Fig. 5c and 5d report the cw-PIA spectra for excitation at 488 nm and 700 nm respectively, which show the very same features, a part from the peak at 760 nm due to the perovskite contribution (Fig. 5c). The MEH-PPV polarons can be clearly recognized in the region around 880 nm together with the onset at 1,050 nm of the low-energy polaron located in the IR region[43,44] for both the excitation wavelengths (Fig. 5c and Fig. 5d). This result supports the hypothesis drafted discussing the polymer PL quenching of a charge-transfer occurring between the two components when exciting both of them. In addition, for the similarity of the obtained spectra, we can conclude that a charge-transfer process also occurs when selectively exciting the perovskite. It is worth noting that the charge-transfer process suggested by spectroscopic evidences confirms the outcome of the KPFM analysis discussed above.

Discussion

In summary, we report on the realization of a polymer-perovskite nanocomposite, which aim to solve some of the issues related to the perovskite deposition on large surfaces toward the mass production
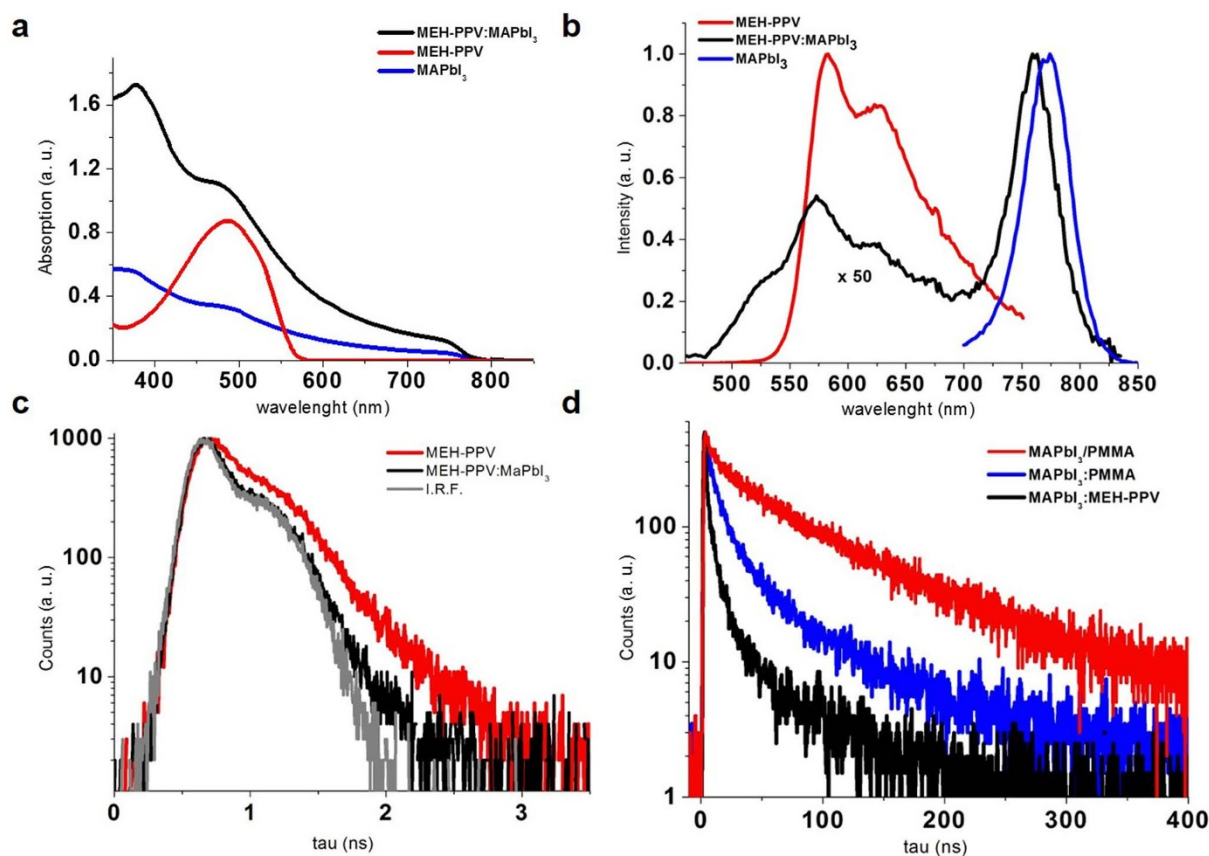
Figure 4 | **Absorption and photoluminescence study of polymer:perovskite film.** (a), Absorption spectra of the two components and the nanocomposite in the device configuration, (b), Steady state photoluminescence of the two pristine materials and the nanocomposite, (c), time resolved PL of the polymer and the nanocomposite collected at 600 nm with 509 nm excitation (d), time resolved PL of the perovskite covered with PMMA, blended with PMMA and blended with the active polymer, collected at 770 nm with 635 nm excitation.

of optoelectronic devices. The templating properties of the polymer are exploited to control the inclusion of small and uniform $MAPbI_3$ domains, allowing the deposition of a smooth film in a single step procedure. This processing improvement represents an ideal additional value foreseeing web processing of optoelectronic devices embedding this blend. As a proof of concept, we demonstrate that the nanocomposite can actively operate in solar cell, leading to a remarkable PV efficiency up to 3%, the highest ever reported for the employed MEH-PPV polymer. Through KPFM and cw-PIA spectroscopy we experimentally demonstrate the photo-physics behind this device, proving an efficient charge transfer mechanism at $MAPbI_3$/polymer interface.

The simplicity of the fabrication approach via one-step deposition and, above all, improved film forming ability over pristine perovskite, provides a novel strategy towards the future implementation of solar cells and, more in general, optoelectronic devices into large scale applications.

The nearly endless combination of on-purpose designed polymers and perovskite materials opens the possibility of a wide development of this research front, towards a continued PV improved efficiency, as well as the potential application of the nanocomposite for other optoelectronic devices such as light emitting diodes and transistors.

Methods

Nanocomposite preparation. The $MAPbI_3$ perovskite was prepared according to the reported procedure[45]. A hydroiodic acid (30 mL, 0.227 mol, 57 wt.% in water, Aldrich) and methylamine (33.7 mL, 0.273 mol, 33% in ethanol, TCI) were stirred under nitrogen atmosphere in the ice bath for 2 h. After stirring at 0°C for 2 h, the resulting solution was evaporated at 50°C for 1 h and produced synthesized chemicals (MAI). Crystallization of MAI was achieved using a rotary evaporator. A white crystalline solid was obtained and washed three times with diethyl ether, dried

in a vacuum oven overnight and used without further purification. To prepare $MAPbI_3$ equimolar mixtures of the readily synthesized MAI (0.234 g) and PbI_2 (0.682 g, 99% Aldrich) were mixed in anhydrous DMF (2 mL, anhydrous 99.8%, Aldrich) at room temperature. The nanocomposite blends were formed by adding a defined volume (ranging from 20 μl to 80 μl) of the 40_{wt}% perovskite precursor solution in DMF, to 100 μl of a 5 mg/ml polymer solution in THF (anhydrous 99.9%, MEH-PPV Mn = 40,000–70,000, purchased Aldrich), and by adding DMF until the final volume of 180 μl. The ratio between perovskite and MEH-PPV ranged from 1 : 18 to 1 : 70 in the final solutions. Finally tBuPy solution (96%Aldrich) was used as additive by adding 0.03% w/w respect to the perovskite precursors. The solution was shaken in screw-capped glass vials at 25°C until equilibrium, under nitrogen atmosphere (in glove-box).

Device fabrication and characterization. FTO/glass substrates (Pilkington, TEC15, 15 Ohm/sq) were etched with metallic Zn and HCl 2M. They were washes with water and cleaned in an ultrasonic bath in acetone and isopropanol for 10 min each. Finally they were immersed into a TL1 washing solution (H_2O_2/NH_3/H_2O 5 : 1 : 1, v/v) and heated to 80°C for 10 min to remove organic contamination, then rinsed 10 times in water. To make a compact TiO_2 blocking layer of ∼90 nm, the cleaned FTO glasses were spin-coated (3,000 rpm) by a double layer of 0.15 M titanium diisopropoxidebis(acetylacetonate) (75% Aldrich) in 1-butanol (Aldrich), then heated at 125°C for 5 min. After coating, the films were cooled down to the room-temperature; finally a third layer of thicker TiO_2 was deposited in the same manner by a 0.3 M titanium diisopropoxidebis(acetylacetonate) solution in 1-butanol. The coated FTO glasses with TiO_2 precursor solutions were heated at 550°C for 2 hours. Nanocomposite blend solutions were deposited onto the compact-TiO_2 electrode film by spin-coating (3,500 rpm for 60 seconds) in N_2 atmosphere. The coated films were then annealed on a hot-plate set at 100°C for 15 minutes. Finally, solar cell devices were completed by thermal evaporation of 5 nm MeO-TPD and 30 nm Au electrodes. All the device areas (∼0.09 cm²) were measured by an optical microscope equipped with a ruler. The devices were characterized under Air Mass 1.5 Global (AM 1.5G) solar simulator with an irradiation intensity of 100 mW·cm⁻². Current–voltage characteristics of the PV devices were studied using a Keithley 2400 Source Measure Unit and a solar simulator Spectra Physics Oriel 150 W with AM1.5G filter set. The integrated intensity was set to 100 mW·cm⁻² using a thermopile radiant power meter with fused-silica window (Spectra Physics Oriel, model 70260). The step
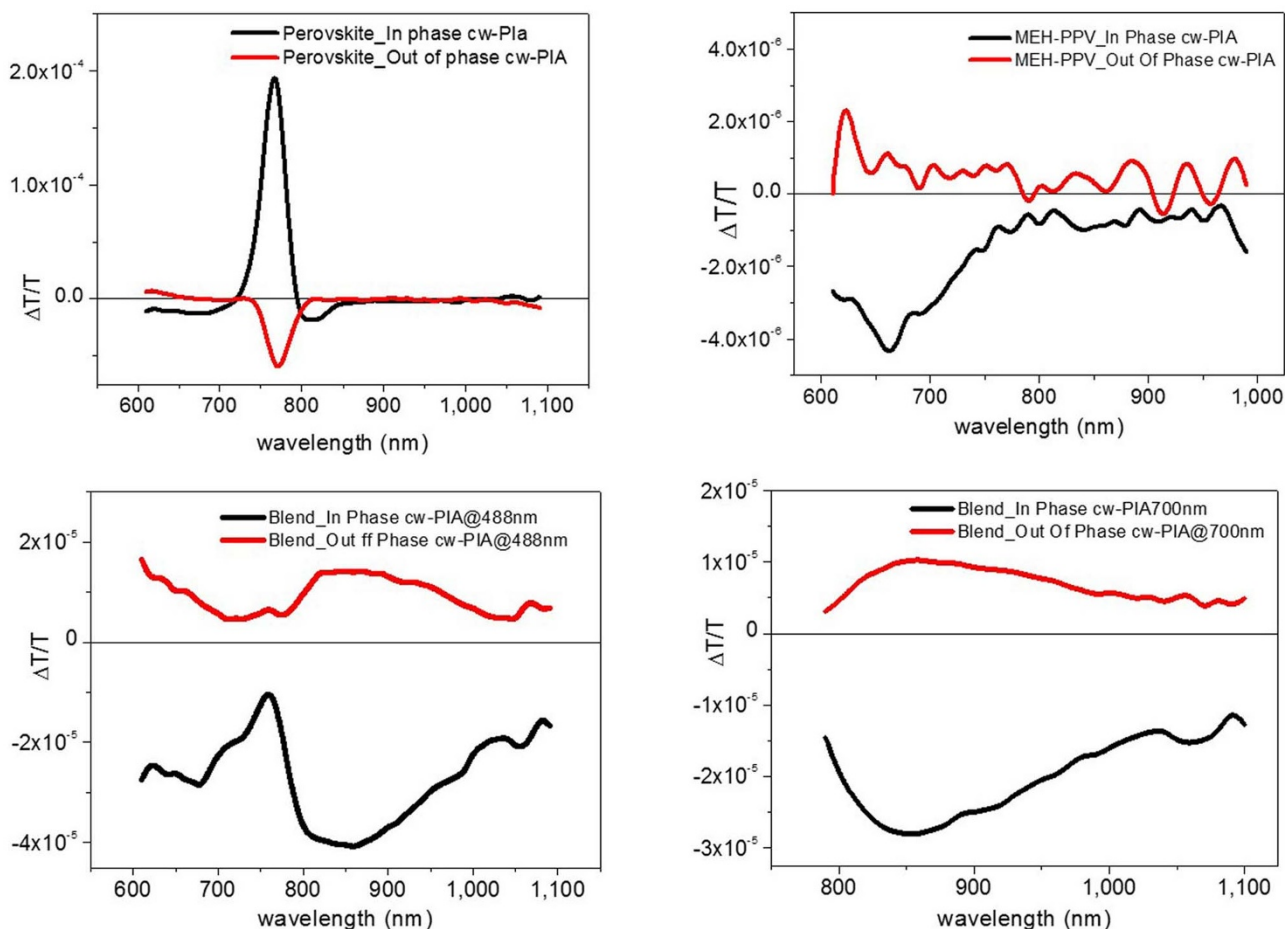
Figure 5 | cw-PIA of model samples on glass substrate. (a), perovskite film, excited with 488 nm laser. (b), MEH-PPV, excited with 488 nm laser. (c), nanocomposite excited at 488 nm. (d), nanocomposite excited at 700 nm.

voltage was fixed at 10 mV and the delay time, which is a set delay at each voltage step before measuring each current, was modulated. J-V curves for all devices were measured by masking the active area with a metal mask 0.09 cm^{-2} in area.

The IPCE was measured using a power source (Newport 300 W xenon lamp, 66920) with a monochromator (Newport Cornerstone 260) and a multimeter (Keithley 2001).

Morphological and structural analysis of the nanocomposite films. The SEM imaging was performed by the MERLIN Zeiss SEM FEG instrument at an accelerating voltage of 5 kV using an In-lens detector. AFM and KPFM measurements were obtained in air by employing a commercial microscope Multimode (Bruker) with Extender Electronics module. In order to obtain a sufficiently large and detectable mechanical deflection, we used (k = 2.8 N·m^{-1}) Pt/Ir coated ultra-lever silicon tips (SCM, Bruker) with oscillating frequencies in the range between 60–90 KHz. AFM and KPFM images are acquired in the same measurement; a topographic line scan is first obtained by AFM operating in Tapping Mode and then that same line is rescanned in Lift Mode with the tip raised to a lift height of 20 nm. KPFM provides a voltage resolution of about 5 mV, while the lateral resolution amounts to a few tens of nanometers. Higher lateral resolution is achieved in AFM amounting to few nanometers. The issue of the lateral resolution[46,47] and the application of AFM/KPFM technique in material science for opto-electronics[48,49] is comprehensively discussed in literature.

The mean square roughness (R$_{rms}$) has been estimated by averaging the values obtained on several 15 × 15 μm^2 images acquired on different regions of the sample (corresponding to about 1,000 μm^2 of sampled surface).

Film thickness was measured by using an Alfa-Step IQ profilometer.

The XRD spectra of the prepared films were measured with a PAN alytical X'Pert-PRO Materials Research Diffractometer using graphite-monochromated CuKα radiation (λ = 1.5405 Å).

Fourier Transform Infrared (FT-IR) spectroscopy measurements in the 4,000–600 cm^{-1} spectral range were carried either on perovskite or nanocomposite deposited onto silicon substrates using a JASCO FT-IR 6300 spectrophotometer in transmission mode at a resolution of 4 cm^{-1}.

Photophysical characterization. Cw-PIA spectra were recorded using a white probe light generated by a 250 W tungsten-halogen lamp which was superimposed to a square-wave modulated laser(spectra physics, 50 mW nominal power, λ = 488 nm) as excitation. The white probe light passed through a first monochromator (Princeton Acton Spectra Pro) before being focused on the sample in a spot of 0.5 cm^2. The light transmitted through the sample was focused onto a second monochromator and detected by a silicon photodiode connected to a current amplifier (femto DLPCA200) and then to a lock-in amplifier (Stanford Research System model SR 830). Intensity of approximately 12 mW·cm^{-2} and modulation frequency of 170 Hz were used for the pump.

Time resolved and steady state photoluminescence measurements were performed using time correlated single photon counting (TCSPC) apparatus of Hamamatsu FL980, 100 ps time resolution with deconvolution analysis. Pulsed excitation sources at 515 nm and 690 nm were employed for time resolved analysis.

Ultraviolet-visible absorption spectra were recorded on Varian Cary 500 spectrophotometer in the 350–1,000 nm wavelength range at room temperature.

Samples used for photophysical characterization were prepared by depositing nanocomposite onto glass and encapsulated with a glass substrate.

1. Zhou, H. *et al.* Photovoltaics. Interface engineering of highly efficient perovskite solar cells. *Science* **345**, 542–546 (2014).
2. Tan, Z. K. *et al.* Bright light-emitting diodes based on organometal halide perovskite. *Nat. Nanotechnol.* **9**, 687–692 (2014).
3. Wehrenfennig, C., Liu, J., Snaith, H. J., Johnston, M. B. & Herz, L. M. Homogeneous Emission Line Broadening in the Organo Lead Halide Perovskite CH$_3$NH$_3$PbI$_{3-x}$Cl$_x$. *J. Phys. Chem. Lett.* **5**, 1300–1306 (2014).
4. Deschler, F. *et al.* High Photoluminescence Efficiency and Optically Pumped Lasing in Solution-Processed Mixed Halide Perovskite Semiconductors. *J. Phys. Chem. Lett.* **5**, 1421–1426 (2014).
5. Xing, G. *et al.* Low-temperature solution-processed wavelength-tunable perovskites for lasing. *Nat. Mater.* **13**, 476–480 (2014).
6. Mitzi, D. B. [Vol. 48] *Progress in Inorganic Chemistry*, [Karlin, K. D. (ed.)] [1–121] ((John Wiley & Sons, USA, 1999).
7. Chen, Q. *et al.* Planar heterojunction perovskite solar cells via vapor-assisted solution process. *J. Am. Chem. Soc.* **136**, 622–625 (2014).
8. Bi, D. Q. *et al.* Using a two-step deposition technique to prepare perovskite (CH$_3$NH$_3$PbI$_3$) for thin film solar cells based on ZrO$_2$ and TiO$_2$ mesostructures. *Rsc Advances* **3**, 18762–18766 (2013).

9. Eperon, G. E., Burlakov, V. M., Docampo, P., Goriely, A. & Snaith, H. J. Morphological Control for High Performance, Solution-Processed Planar Heterojunction Perovskite Solar Cells. *Adv.Funct.Mat.* **24**, 151–157 (2013).

10. Wei, Z., Chen, H., Yan, K. & Yang, S. Inkjet Printing and Instant Chemical Transformation of a $CH_3NH_3PbI_3$/Nanocarbon Electrode and Interface for Planar Perovskite Solar Cells. *Angew. Chem.* **126**, 13455–13459 (2014).

11. Barrows, A. T. *et al.* Efficient planar heterojunction mixed-halide perovskite solar cells deposited via spray-deposition. *Energy Environ. Sci.* **7**, 2944–2950 (2014).

12. You, J. *et al.* A polymer tandem solar cell with 10.6% power conversion efficiency. *Nat. Commun.* **4**, 1446 (2013).

13. Ross, R. B. *et al.* Endohedral fullerenes for organic photovoltaic devices. *Nat. Mater.* **8**, 208–212 (2009).

14. Scharber, M. C. *et al.* Design Rules for Donors in Bulk-Heterojunction Solar Cells- Towards 10 % Energy-Conversion Efficiency. *Adv. Mater.* **18**, 789–794 (2006).

15. Boschloo, G. & Hagfeldt, A. Photoinduced absorption spectroscopy of dye-sensitized nanostructured TiO_2. *Chem. Phys. Lett.* **370**, 381–386 (2003).

16. Nonnenmacher, M., Oboyle, M. P. & Wickramasinghe, H. K. Kelvin Probe Force Microscopy. *Appl. Phys. Lett.* **58**, 2921–2923 (1991).

17. Sariciftci, N. S. *et al.* Semiconducting polymer-buckminsterfullerene heterojunctions: Diodes, photodiodes, and photovoltaic cells. *Appl. Phys. Lett.* **62**, 585 (1993).

18. Burroughes, J. H. *et al.* Light-emitting diodes based on conjugated polymers. *Nature* **347**, 539–541 (1990).

19. Sirringhaus, H., Tessler, N. & Friend, R. H. Integrated optoelectronic devices based on conjugated polymers. *Science* **280**, 1741–1744 (1998).

20. Boschloo, G., Haggman, L. & Hagfeldt, A. Quantification of the effect of 4-tert-butylpyridine addition to I^-/I_3^- redox electrolytes in dye-sensitized nanostructured TiO_2 solar cells. *J. Phys. Chem. B* **110**, 13144–13150 (2006).

21. Jeon, N. J. *et al.* Solvent engineering for high-performance inorganic-organic hybrid perovskite solar cells. *Nat. Mater.* **13**, 897–903 (2014).

22. Colella, S. *et al.* $MAPbI_{3-x}Cl_x$ Mixed Halide Perovskite for Hybrid Solar Cells: The Role of Chloride as Dopant on the Transport and Structural Properties. *Chem. Mater.* **25**, 4613–4618 (2013).

23. Xue, L., Cheng, Z., Fu, J. & Han, Y. Dewetting behavior of polystyrene film filled with $(C_6H_5C_2H_4NH_3)_2PbI_4$. *J. Chem. Phys.* **129**, 054905 (2008).

24. Li, W. Z. *et al.* Montmorillonite as bifunctional buffer layer material for hybrid perovskite solar cells with protection from corrosion and retarding recombination. *J. Mater. Chem. A* **2**, 13587–13592 (2014).

25. Jie, L., Tzung-Fang, G. & Yang, Y. Effects of thermal annealing on the performance of polymer light emitting diodes. *J. Appl. Phys.* **91**, 1595 (2002).

26. Jin, H. *et al.* Effect of molecular aggregation by thermal treatment on photovoltaic properties of MEH-PPV: Fullerene-based solar cells. *Sol. Energ. Mat. Sol. C.* **93**, 289–294 (2009).

27. Chavhan, S. *et al.* Organo-metal halide perovskite-based solar cells with CuSCN as the inorganic hole selective contact. *J. Mater. Chem. A* **2**, 12754–12760 (2014).

28. Juarez-Perez, E. J. *et al.* Role of the Selective Contacts in the Performance of Lead Halide Perovskite Solar Cells. *J. Phys. Chem. Lett.* **5**, 680–685 (2014).

29. Chang, E. C., Chao, C. I. & Lee, R. H. Enhancing the efficiency of MEH-PPV and PCBM based polymer solar cells via optimization of device configuration and processing conditions. *J. Appl. Polym. Sci.* **101**, 1919–1924 (2006).

30. Yan, Q. X. *et al.* Improved Photovoltaic Performance of MEH-PPV/PCBM Solar Cells via Incorporation of Si Nanocrystals. *Chinese J. Chem.* **31**, 1380–1384 (2013).

31. Habisreutinger, S. N. *et al.* Carbon Nanotube/Polymer Composites as a Highly Stable Hole Collection Layer in Perovskite Solar Cells. *Nano Lett.* **14**, 5561–5568 (2014).

32. Juarez-Perez, E. J. *et al.* Photoinduced Giant Dielectric Constant in Lead Halide Perovskite Solar Cells. *J. Phys. Chem. Lett.* **5**, 2390–2394 (2014).

33. Snaith, H. J. *et al.* Anomalous Hysteresis in Perovskite Solar Cells. *J. Phys. Chem. Lett.* **5**, 1511–1515 (2014).

34. Ungera, E. L. *et al.* Hysteresis and transient behavior in current-voltage measurements of hybrid-perovskite absorber solar cells. *Energy Environ. Sci.* **7**, 3690–3698 (2014).

35. Liscio, A. *et al.* Photovoltaic Charge Generation Visualized at the Nanoscale: A Proof of Principle. *J. Am. Chem. Soc.* **130**, 780–781 (2008).

36. Arango, A. C., Carter, S. A. & Brock, P. J. Charge transfer in photovoltaics consisting of interpenetrating networks of conjugated polymer and TiO_2 nanoparticles. *Appl. Phys. Lett.* **74**, 1698–1700 (1999).

37. Smilowitz, L., Hays, A., Heeger, A. J., Wang, G. & Bowers, J. E. Timeresolved photoluminescence from poly[2methoxy, 5(2′ethylhexyloxy)p-phenylenevinylene]: Solutions, gels, films, and blends. *J. Chem. Phys.* **98**, 6504 (1993).

38. Zhang, W. *et al.* Enhancement of perovskite-based solar cells employing core-shell metal nanoparticles. *Nano Lett.* **13**, 4505–4510 (2013).

39. Roiati, V. *et al.* Stark effect in perovskite/TiO_2 solar cells: evidence of local interfacial order. *Nano Lett.* **14**, 2168–2174 (2014).

40. Choi, J. J., Yang, X. H., Norman, Z. M., Billinge, S. J. L. & Owen, J. S. Structure of Methylammonium Lead Iodide Within Mesoporous Titanium Dioxide: Active Material in High-Performance Perovskite Solar Cells. *Nano Lett.* **14**, 127–133 (2014).

41. Roiati, V. *et al.* Investigating charge dynamics in halide perovskitesensitized mesostructured solar cells. *Energy Environ. Sci.* **7**, 1889–1894 (2014).

42. Lee, C. L., Hwang, I. W., Byeon, C. C., Kim, B. H. & Greenham, N. C. Triplet Exciton and Polaron Dynamics in Phosphorescent Dye Blended Polymer Photovoltaic Devices. *Adv. Funct. Mater.* **20**, 2945–2950 (2010).

43. Smilowitz, L. *et al.* Photoexcitation spectroscopy of conducting-polymer -C_{60} composites: Photoinduced electron transfer. *Phys. Rev. B* **47**, 13835–13842 (1993).

44. Janssen, R. A. J. *et al.* Photoinduced electron transfer reactions in mixed films of p-conjugated polymers and a homologous series of tetracyano-p-quinodimethane derivatives. *J Chem. Phys.* **103**, 8840–8845 (1995).

45. Lee, M. M., Teuscher, J., Miyasaka, T., Murakami, T. N. & Snaith, H. J. Efficient hybrid solar cells based on meso-superstructured organometal halide perovskites. *Science* **338**, 643–647 (2012).

46. Liscio, A., Palermo, V. & Samori, P. Probing local surface potential of quasi-one-dimensional systems: A KPFM study of P3HT nanofibers. *Adv. Funct. Mater.* **18**, 907–914 (2008).

47. Liscio, A., Palermo, V. & Samori, P. Nanoscale quantitative measurement of the potential of charged nanostructures by electrostatic and Kelvin probe force microscopy: unraveling electronic processes in complex materials. *Acc. Chem. Res.* **43**, 541–550 (2010).

48. Melitz, W., Shen, J., Kummel, A. C. & Lee, S. Kelvin probe force microscopy and its application. *Surf. Sci. Rep.* **66**, 1–27 (2011).

49. Musumeci, C., Liscio, A., Palermo, V. & Samorì, P. Electronic characterization of supramolecular materials at the nanoscale by Conductive Atomic Force and Kelvin Probe Force microscopies. *Mater. Today*, DOI: 10.1016/j.mattod.2014.05.010 (2014).

Acknowledgments

Author contributions

S.C., A.R. and S.M. conceived the experiments, data analysis and interpretation. S.M. performed the fabrication of devices, device performance measurements and characterization. S.C. prepared the materials for perovskites and performed the FT-IR and XRD characterization. A.R. performed the SEM characterization. V.R. and A.L.T. carried out the photophysical analysis. A.L.S. and V.P. performed AFM/KPFM characterization. The manuscript was written by S.M., A.R. and S.C. The project was planned, directed and supervised by S.C., A.R. and G.G. All authors discussed the results and commented on the manuscript.

Additional information